Journal of Computational Physics **168,** 101–133 (2001)
doi:10.1006/jcph.2000.6683, available online at http://www.idealibrary.com on IDEAL®

A High-Resolution Pressure-Based Algorithm for Fluid Flow at All Speeds

F. Moukalled and M. Darwish

Faculty of Engineering & Architecture, Mechanical Engineering Department, American University of Beirut, P.O. Box 11-0236, Beirut, Lebanon
E-mail: memouk@aub.edu.lb, darwish@aub.edu.lb

Received June 16, 1999; revised November 28, 2000

A new collocated finite-volume-based solution procedure for predicting viscous compressible and incompressible flows is presented. The technique is equally applicable in the subsonic, transonic, and supersonic regimes. Pressure is selected as a dependent variable in preference to density because changes in pressure are significant at all speeds as opposed to variations in density, which become very small at low Mach numbers. The newly developed algorithm has two new features: (i) the use of the normalized variable and space formulation (NVSF) methodology to bound the convective fluxes and (ii) the use of a high-resolution scheme in calculating interface density values to enhance the shock-capturing property of the algorithm. The virtues of the newly developed method are demonstrated by solving a wide range of flows spanning the subsonic, transonic, and supersonic spectrum. Results obtained indicate higher accuracy when calculating interface density values using a high-resolution scheme.

Key Words: finite-volume method; all speed flows; pressure-based algorithm; high-resolution schemes.

INTRODUCTION

In computational fluid dynamics (CFD), great research efforts have been devoted to the development of accurate and efficient numerical algorithms suitable for solving flows in the various Reynolds and Mach number regimes. The type of convection scheme to be used in a given application depends on the value of Reynolds number. For low Reynolds number flows, the central difference or hybrid scheme is adequate [1]. In dealing with flows of high Reynolds number, numerous discretization schemes for the convection term arising in the transport equations have been employed [2–11]. On the other hand, the Mach number value dictates the type of algorithm to be utilized in the solution procedure. These algorithms can be divided into two groups: density-based methods and pressure-based methods, with the former used for high Mach number flows, and the latter for low Mach number flows. In

0021-9991/01 $35.00

density-based methods, continuity is employed as an equation for density, and pressure is obtained from an equation of state. In pressure-based methods, continuity is utilized as a constraint on velocity and is combined with momentum to form a Poisson-like equation for pressure. Each of these methods is appropriate for a specific range of Mach number values.

The ultimate goal, however, is to develop a unified algorithm capable of solving flow problems in the various Reynolds and Mach number regimes. To understand the difficulty associated with the design of such an algorithm, it is important to understand the role of pressure in a compressible fluid flow [12]. In the low Mach number limit where density becomes constant, the role of pressure is to act on velocity through continuity so that conservation of mass is satisfied. Obviously, for low speed flows, the pressure gradient needed to drive the velocities through momentum conservation is of such magnitude that the density is not significantly affected and the flow can be considered nearly incompressible. Hence, density and pressure are very weakly related. As a result, the continuity equation is decoupled from the momentum equations and can no longer be considered as the equation for density. Rather, it acts as a constraint on the velocity field. Thus, for a sequential solution of the equations, it is necessary to devise a mechanism to couple the continuity and momentum equations through the pressure field. In the hypersonic limit where variations in velocity become relatively small as compared to the velocity itself, the changes in pressure do significantly affect density. In this limit, the pressure can be viewed to act on density alone through the equation of state so that mass conservation is satisfied [12], and the continuity equation can be viewed as the equation for density. This view of the two limiting cases of compressible flow can be generalized in the following manner. In compressible flow situations, the pressure takes on a dual role to act on both density and velocity through the equation of state and momentum conservation, respectively, so that mass conservation is satisfied. For a subsonic flow, mass conservation is more readily satisfied by pressure influencing velocity than by pressure influencing density. For a supersonic flow, mass conservation is more readily satisfied by pressure influencing density than by pressure influencing velocity.

The above discussion reveals that for any numerical method to be capable of predicting both incompressible and compressible fluid flow, the pressure should always be allowed to play its dual role and to act on both velocity and density to satisfy continuity. Nevertheless, through the use of the so-called pseudo or artificial compressibility technique [13, 14], several density-based methods for fluid flow at all speeds have been developed. These methods encountered difficulties in efficiently avoiding the stiff solution matrices that greatly degraded their rate of convergence. To overcome this problem and ensure convergence over all speed ranges, preconditioning of the resulting stiff matrices was introduced and several methods (e.g., Turkel [15], Choi and Merkle [16], Turkel *et al.* [17], Tweedt *et al.* [18], Van Leer *et al.* [19], Weiss and Smith [20], Merkle *et al.* [21], and Edwards and Liou [22] to cite a few) using this promising technique have appeared in the literature. Recently, Turkel [23] presented an extensive review of the preconditioners given by Turkel [15, 24], Choi and Merkle [16], and Van Leer *et al.* [19].

At the other frontier, several researchers [12, 25–40] have worked on extending the range of pressure-based methods, with various degrees of success, to high Mach numbers following either a staggered grid approach [12, 25–27] or a collocated variable formulation [28–35]. The method of Shyy and Chen [26], developed within a multigrid environment, uses a second-order upwind scheme in discretizing the convective terms. Moreover, at high Mach number values, a first-order upwind scheme is employed for evaluating the density at

the control volume faces. Yang *et al.* [28] used a general strong conservation formulation of the momentum equations that allows several forms of the velocity components to be chosen as dependent variables. In the method developed by Marchi and Maliska [29], values for density, convection fluxes, and convection-like terms at the control volume faces are calculated using the upwind scheme. Demirdzic *et al.* [30], however, used a central difference scheme blended with the upwind scheme to evaluate these quantities. Lien and Leschziner [31, 32] adopted the streamwise-directed density-retardation concept, which is controlled by Mach-number-dependent monitor functions, to account for the hyperbolic character of the conservation laws in the transonic and supersonic regimes. Politos and Giannakoglou [33] developed a pressure-based algorithm for high-speed turbomachinery flows also following the retarded density concept. In their method, unlike the work of Lien and Leschziner [31, 32], the retarded density operates only on the velocity component correction during the pressure-correction phase. Chen and Pletcher [34] developed a coupled modified strongly implicit procedure that uses the strong conservation forms of Navier–Stokes equations with primitive variables. Issa and Javareshkian [35] introduced a pressure-based compressible calculation method, using Tatal Variation Diminishing (TVD) schemes, that has a resolution quality similar to that obtained when applied in density-based methods. The methods of Karimian and Schneider [36–38] and Darbandi and Schneider [39, 40] are formulated within a control-volume-based finite element framework. While Karimian and Schneider [36–38] used primitive variables in their formulation, Darbandi and Schneider [39, 40] employed the momentum components as dependent variables.

From the aforementioned literature review, it is obvious that in most of the published work the first-order upwind scheme is used to interpolate for density when in the source of the pressure correction equation; an exception occurs in the work presented in [30–33] where a central difference method is adopted. In the technique developed by Demirdzic *et al.* [30], the second-order central difference scheme blended with the upwind scheme is used. The bleeding relies on a factor varying between 0 and 1. In the work presented in [31–33], the retarted density concept is utilized in calculating the density at the control volume faces. This concept is based on factors that are problem-dependent and requires the addition of some artificial dissipation to stabilize the algorithm (second-order terms were introduced), which complicate its use.

To this end, the objective of this paper is to present a newly developed pressure-based solution procedure that is equally valid at all Reynolds and Mach number values. The collocated variable algorithm is formulated on a nonorthogonal coordinate system using Cartesian velocity components. The method is easy to implement, highly accurate, and does not require any explicit addition of damping terms to stabilize it or to properly resolve shock waves. Moreover, the algorithm has two new features. The first one is the use of the normalized variable formulation (NVF) [41] and/or the normalized variable and space formulation (NVSF) [42] methodology in the discretization of the convective terms. To the authors' knowledge, the NVF/NVSF methodologies have never been used to bound the convective flux in compressible flows. Mainly low-order schemes or the TVD [35, 43] formulation have been adopted. The second one is the use of high-resolution (HR) schemes in the interpolation of density appearing in the mass fluxes in order to enhance the shock-capturing capability of the method.

In what follows, the governing equations for compressible flows are presented and their discretization detailed to lay the groundwork for the derivation of the pressure-correction equation. Then, the increase in accuracy with the use of HR schemes for density is

demonstrated. This is done by comparing predictions, for a number of problems, obtained using the third-order SMART scheme [8] for all variables except density (for which the upwind [1] scheme is used) against another set of results obtained using the SMART scheme for all variables including density.

GOVERNING EQUATIONS

The equations governing the flow of a two-dimensional compressible fluid are the continuity equation, the Δ momentum equations, and the energy equation. This set of nonlinear, coupled equations is solved for the unknowns ρ, $\mathbf{v}$, T, and P. In vector form, these equations may be written as

$$\frac{\partial \rho}{\partial t} + \nabla \cdot (\rho \mathbf{v}) = 0 \tag{1}$$

$$\frac{\partial (\rho \mathbf{v})}{\partial t} + \nabla \cdot (\rho \mathbf{v}\mathbf{v}) = -\nabla P + \nabla \cdot (\mu \nabla \mathbf{v}) + \frac{1}{3}\nabla(\mu \nabla \cdot \mathbf{v}) \tag{2}$$

$$\frac{\partial (\rho T)}{\partial t} + \nabla \cdot (\rho \mathbf{v} T) = \frac{1}{c_P}\left\{ \nabla \cdot (k \nabla T) + \beta T \left[\frac{\partial P}{\partial t} + \nabla \cdot (P\mathbf{v}) - P \nabla \cdot (\mathbf{v}) \right] + \Phi + \dot{q} \right\}, \tag{3}$$

where

$$\Phi = \mu \left\{ 2 \left[\left(\frac{\partial u}{\partial x} \right)^2 + \left(\frac{\partial v}{\partial y} \right)^2 \right] + \left(\frac{\partial u}{\partial y} + \frac{\partial v}{\partial x} \right)^2 - \frac{2}{3} (\nabla \cdot \mathbf{v})^2 \right\} \tag{4}$$

and β is the thermal expansion coefficient, which is equal to $1/T$ for an ideal gas. In addition to the above differential equations, an auxiliary equation of state relating density to pressure and temperature ($\rho = f(P, T)$) is needed. For an ideal gas, this equation is given by

$$\rho = \frac{P}{RT} = C_\rho P, \tag{5}$$

where R is the gas constant.

A review of the above differential equations reveals that they are similar in structure. If a typical representative variable is denoted by ϕ, the general differential equation may be written as

$$\frac{\partial (\rho \phi)}{\partial t} + \nabla \cdot (\rho \mathbf{v} \phi) = \nabla \cdot (\Gamma^\phi \nabla \phi) + Q^\phi, \tag{6}$$

where the expressions for Γ^ϕ and Q^ϕ can be deduced from the parent equations. The four terms in the above equation describe successively unsteadiness, convection (or advection), diffusion, and generation/dissipation effects. In fact, all terms not explicitly accounted for in the first three terms are included in the catchall source term Q^ϕ.

FINITE VOLUME DISCRETIZATION

The general transport equation (Eq. (6)) is discretized using the control volume methodology. For that purpose, Eq. (6) is integrated over the control volume shown in Fig. 1a to

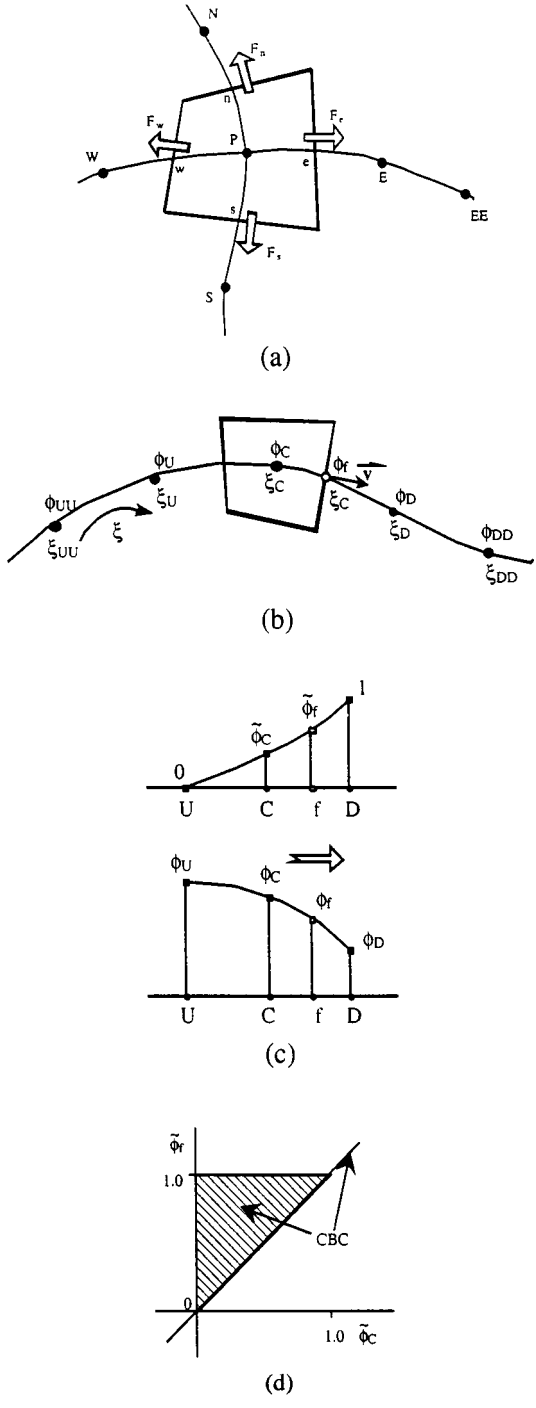

FIG. 1. (a) Control volume; (b) control volume nodes; (c) normalization; (d) CBC.

yield, upon applying the divergence theorem, the discretized equation

$$\frac{\partial}{\partial t}[(\rho\phi)_P]\Omega + \Delta[(\rho\mathbf{v}\phi - \Gamma^\phi \Delta\phi)\cdot\mathbf{S}]_P = Q^\phi\Omega. \tag{7}$$

In the above equation, the Δ operator is the discretized version of the surface integral defined by

$$\Delta[\phi]_P = \phi_e + \phi_w + \phi_n + \phi_s. \tag{8}$$

Hence, Eq. (7) can be written as

$$\frac{\partial}{\partial t}[(\rho\phi)_P]\Omega + \Delta[J]_P = \frac{\partial}{\partial t}[(\rho\phi)_P]\Omega + (J_e + J_w + J_n + J_s) = Q^\phi\Omega. \tag{9}$$

In Eq. (9), J_f represents the total flux of ϕ across face "f" and is given by

$$J_f = (\rho\mathbf{v}\phi - \Gamma^\phi\nabla\phi)_f\cdot\mathbf{S}_f, \tag{10}$$

where $\mathbf{S}_f$ is the surface vector of cell face "f." The flux J_f is a combination of the convection flux $J_f^c = (\rho\mathbf{v}\phi)_f\cdot\mathbf{S}_f$ and diffusion flux $J_f^D = (-\Gamma^\phi\nabla_\phi)_f\cdot\mathbf{S}_f$.

From Eq. (9), it is obvious that the total fluxes are needed at the control volume faces where the values of the dependent variables are not available and that they should be obtained by interpolation. Therefore, the accuracy of the solution depends on the proper estimation of these values as a function of the neighboring ϕ node values.

The discretization of the diffusion flux J_f^D does not require any special consideration and the method adopted here is described in Zwart *et al.* [44].

The discretization of the convection flux is, however, problematic and requires special attention. The convection flux of ϕ through the control volume face "f" may be written as

$$J_f^C = (\rho\mathbf{v}\phi)_f\cdot\mathbf{S}_f = F_f\phi_f, \tag{11}$$

where ϕ_f stands for the mean value of ϕ along cell face "f," and $F_f = (\rho\mathbf{v}\cdot\mathbf{S})_f$ is the mass flow rate across face f. Using some assumed interpolation profile, ϕ_f can be explicitly formulated by a functional relationship of the form

$$\phi_f = f(\phi_{NB}), \tag{12}$$

where ϕ_{NB} denotes the ϕ values at the neighboring nodes. The interpolation profile should be bounded in order not to give rise to the well-known dispersion error problem [2]. In this work, HR schemes formulated in the context of the NVSF methodology, which is explained in the next section, are used. For the representation of the unsteady term, the grid-point value of ϕ is assumed to prevail throughout the control volume, and the time derivative is approximated using a Euler-implicit formulation.

The discretized equation, Eq. (9), is transformed into an algebraic equation at the main grid point P by substituting the fluxes at all faces of the control volume by their equivalent expressions. Then, performing some algebraic manipulations on the resultant equation,

the following algebraic relation, linking the value of the dependent variable at the control volume center to the neighboring values, is obtained:

$$a_P^{\phi}\phi_P = \sum_{NB(P)} a_{NB}^{\phi}\phi_{NB} + b_P^{\phi}. \tag{13}$$

For the solution domain as a whole a system of N equations in N unknown results, where N is the number of control volumes. Owing to the nonlinear nature of the set of equations, the discretized equations are solved by the use of iterative methods. The algorithm used in this work is the Tri-Diagonal Matrix Algorithm (TDMA) [45].

THE NVSF METHODOLOGY FOR CONSTRUCTING HR SCHEMES

As mentioned earlier, the discretization of the convection flux is not straightforward and requires additional attention. Since the intention is to develop a high-resolution algorithm, the highly diffusive first-order upwind scheme [1] is excluded. As such, a high-order interpolation profile is sought. The difficulties associated with the use of such profiles stem from the conflicting requirements of accuracy, stability, and boundedness. Solutions predicted with high-order profiles tend to provoke oscillations in the solution when the local Peclet number is high in combination with steep gradients of the flow properties. To suppress these oscillations, many techniques have been advertised and may be broadly classified into two groups: the flux blending method [46–49] and the composite flux limiter method [8, 41–43, 50]. The latter is the one adopted here. In this technique, the numerical flux at the interface of the computational cell is modified by employing a flux limiter that enforces boundedness. The formulation of high-resolution flux limiter schemes on uniform grid has recently been generalized by Leonard [41, 50] through the normalized variable formulation (NVF) methodology and on nonuniform grid by Darwish and Moukalled [42] through the normalized variable and space formulation (NVSF) methodology. The NVF and NVSF methodologies have provided a good framework for the development of HR schemes that combine simplicity of implementation with high accuracy and boundedness. Moreover, to the authors' knowledge, the NVSF formulation has never been used to bound the convection flux in compressible flows. It is an objective of this work to extend the applicability of this technique to compressible flows. Therefore, before introducing the high-resolution algorithm, a brief review of the NVSF methodology is in order.

Figure 1b shows the local behavior of the convected variable near a control-volume face. The node labeling refers to the upstream, central, and downstream grid points designated by U, C, and D, located at distances ξ_U, ξ_C, and ξ_D from the origin, respectively. The values of ϕ at these nodes are designated by ϕ_U, ϕ_C, and ϕ_D, respectively. Moreover, the value of the dependent variable at the control volume face located at a distance ξ_f from the origin is expressed by ϕ_f. With this notation, the normalized variables are defined as

$$\tilde{\phi} = \frac{\phi - \phi_U}{\phi_D - \phi_U} \quad \tilde{\xi} = \frac{\xi - \xi_U}{\xi_D - \xi_U}. \tag{14}$$

The use of the above-normalized parameters simplifies the functional representation of interpolation schemes (Fig. 1c) and helps define the stability and boundedness conditions that they should satisfy.

Based on the normalized variable analysis, Gaskell and Lau [8] formulated a convection boundedness criterion (CBC) for implicit steady flow calculation. This CBC states that for a scheme to have the boundedness property, its functional relationship should be continuous, it should be bounded from below by $\tilde{\phi}_f = \tilde{\phi}_C$ and from above by unity, and in the monotonic range ($0 < \tilde{\phi}_C < 1$), it should pass through the points (0,0) and (1,1), and for $1 < \tilde{\phi}_C$ or $\tilde{\phi}_C < 0$, the functional relationship $f(\tilde{\phi}_C)$ should equal $\tilde{\phi}_C$. These conditions are shown graphically in Fig. 1d.

Knowing the required conditions for boundedness, the shortcomings of high-order (HO) schemes were eliminated through the development of HR schemes satisfying all above requirements. Without going into detail, a number of HR schemes were formulated using the NVF/NVSF methodologies, and the functional relationship for the SMART scheme [8] extensively used in this work is given by

$$\tilde{\phi}_f = \begin{cases} \frac{\tilde{\xi}_f(1-3\tilde{\xi}_C+2\tilde{\xi}_f)}{\tilde{\xi}_C(1-\tilde{\xi}_C)}\tilde{\phi}_C & 0 < \tilde{\phi}_C < \frac{\tilde{\xi}_C}{3} \\ \frac{\tilde{\xi}_f(1-\tilde{\xi}_f)}{\tilde{\xi}_C(1-\tilde{\xi}_C)}\tilde{\phi}_C + \frac{\tilde{\xi}_f(\tilde{\xi}_f-\tilde{\xi}_C)}{1-\tilde{\xi}_C} & \frac{\tilde{\xi}_C}{3} \le \tilde{\phi}_C < \frac{\tilde{\xi}_C}{\tilde{\xi}_f}(1+\tilde{\xi}_f-\tilde{\xi}_C) \\ 1 & \frac{\tilde{\xi}_C}{\tilde{\xi}_f}(1+\tilde{\xi}_f-\tilde{\xi}_C) \le \tilde{\phi}_C < 1 \\ \tilde{\phi}_C & \text{elsewhere.} \end{cases} \tag{15}$$

For more details the reader is referred to Darwish and Moukalled [42].

HIGH-RESOLUTION ALGORITHM

The need for a solution algorithm arises in the simulation of flow problems because a scalar equation does not exist for pressure. Rather, the pressure field acts indirectly on the velocity field to constrain it to satisfy the continuity equation. Hence, if a segregated approach is to be adopted, coupling among the u, v, ρ, and P primitive variables in the continuity and momentum equations will be required. Evidently, the whole set of equations could be solved directly (after linearization) since the number of equations equals the number of unknowns. However, the computational effort and storage requirements needed by such an approach are often prohibitive. This has forced researchers to seek less expensive methods and resulted in the development of several segregated solution algorithms [1, 51–57]. Recently, Moukalled and Darwish presented a unified formulation of these algorithms [58].

The segregated algorithm adopted in this work is the SIMPLE algorithm [1, 51], which involves a predictor and a corrector step. In the predictor step, the velocity field is calculated based on a guessed or estimated pressure field. In the corrector step, a pressure (or a pressure-correction) equation is derived and solved. Then, the variation in the pressure field is accounted for within the momentum equations by corrections to the velocity and density fields. Thus, the velocity, density, and pressure fields are driven, iteratively, to better satisfying the momentum and continuity equations simultaneously and convergence is achieved by repeatedly applying the procedure described above.

Before presenting the pressure-correction equation, the discretized momentum equations are first written in the notationally more suitable form

$$\mathbf{v}_P - \mathbf{H}[\mathbf{v}]_P = -\mathbf{D}_P(\nabla P)_P, \tag{16}$$

where

$$\mathbf{H}[\mathbf{v}]_P = \begin{bmatrix} H[u]_P \\ H[v]_P \end{bmatrix} \quad \mathbf{D}_P = \begin{bmatrix} D[u]_P & 0 \\ 0 & D[v]_P \end{bmatrix} \quad (\nabla P)_P = \begin{bmatrix} (\nabla P)_P \cdot \mathbf{i} \\ (\nabla P)_P \cdot \mathbf{J} \end{bmatrix} = \begin{bmatrix} (\nabla P)_P^x \\ (\nabla P)_P^y \end{bmatrix} \quad (17)$$

$$(\nabla P)_P = \frac{1}{\Omega} \int_\Omega \nabla P \, d\Omega \quad H[\phi]_P = \frac{\sum_{NB(P)} a_{NB}^\phi \phi_{NB} + b_P^\phi}{a_P^\phi} \quad D[\phi]_P = \frac{\Omega}{a_P^\phi}. \quad (18)$$

In the above equations, Ω is the volume of cell P, and the subscripts e, w, n, and s refer to values at the east, west, north, and south faces of the control volume (Fig. 1a).

For the calculation of the mass fluxes across the control volume faces ($U_f = \mathbf{v}_f \cdot \mathbf{S}_f$) and for checking mass conservation, the values of the velocity components are needed there. In order to avoid oscillations which may result if a simple linear interpolation method is used, a special interpolation practice is employed as suggested by Rhie [59], Peric [48], and Majumdar [60].

The Pressure-Correction Equation

As mentioned earlier, the convergence in the segregated approach is driven by the corrector stage where a pressure (or a pressure-correction) equation is solved. Therefore, the first phase in developing a segregated solution algorithm is to derive such an equation. Following the SIMPLE procedure, the momentum and continuity equations are combined to yield the pressure-correction equation, which, in discretized form can be written as

$$\frac{\Omega C_P}{\delta t} P'_P + \Delta[C_\rho U^* P']_P - \Delta[\rho^* \mathbf{D}(\nabla P') \cdot \mathbf{S}]_P = -\frac{(\rho_P^* - \rho_P^\circ)}{\partial t}\Omega - \Delta[\rho^* U^*]_P. \quad (19)$$

From the above equation, it is clear that the starred continuity equation appears as a source term in the pressure-correction equation. Moreover, in a pressure-based algorithm, the pressure-correction equation is the most important equation that gives the pressure, upon which all other variables are dependent. Therefore, the accuracy of the predictions depends on the proper estimation of pressure from this equation. Definitely, the more accurate the interpolated starred density (ρ^*) values at the control volume faces are, the more accurate the predicted pressure values will be. The use of a central difference scheme for the interpolation of ρ^* leads to instability at Mach numbers near or above 1 [12, 27]. On the other hand, the use of a first-order upwind scheme leads to excess diffusion [27]. The obvious solution to the aforementioned problems would be to interpolate for values of ρ^* at the control volume faces in the same way interpolation for other dependent variables is carried out; in other words, the solution would be to employ the bounded HR family of schemes for which no problem-dependent factors are required. Adopting this strategy, the discretized form of the starred steady continuity equation becomes

$$\Delta[\rho^* U^*]_P = (\rho_e^*)^{HR} U_e^* + (\rho_w^*)^{HR} U_w^* + (\rho_n^*)^{HR} U_n^* + (\rho_s^*)^{HR} U_s^*. \quad (20)$$

The same procedure is also adopted for calculating the density when computing the mass flow rate at a control volume face in the general conservation equation.

Upon discretizing the pressure-correction equation (19), an algebraic equation similar to Eq. (13) is obtained at every grid point in the domain. The collection of these equations forms a system that is solved to obtain the pressure-correction field.

BOUNDARY CONDITIONS

The solutions to the above system of equations require the specification of boundary conditions of which several types are encountered in flow calculations, such as inflow, outflow, and no-flow (impermeable walls and symmetry lines). Details regarding the various types and their implementation for both incompressible and compressible flow calculations are well documented in the literature and will not be repeated here. However, it should be stressed that the convergence of the computations greatly depends on the proper implementation of these conditions.

RESULTS AND DISCUSSION

The validity of the solution procedure just described is demonstrated in this section by presenting solutions to the following four inviscid test cases: (i) flow in a converging–diverging nozzle, (ii) flow over a bump, (iii) supersonic flow over a step, and (iv) the unsteady duct filling problem. For all problems, unless otherwise stated, computations were terminated when the maximum residual over the domain and for all dependent variables fell below 10^{-5}.

Flow in a Converging–Diverging Nozzle

The first test selected is a standard one that has been used by several researchers for comparison purposes [30, 31]. The problem is first solved using a pseudo-one-dimensional variable area code. The cross-sectional area of the nozzle varies as

$$S_{(x)} = S_{th} + (S_i - S_{th})\left(1 - \frac{x}{5}\right)^2, \tag{21}$$

where $S_i = 2.035$ and $S_{th} = 1$ are the inlet and throat areas, respectively, and $0 \leq x \leq 10$. Solutions are obtained over a wide range of inlet Mach numbers ranging from the incompressible limit ($M = 0.1$) to supersonic ($M = 7$), passing through transonic with strong normal shock waves, and are presented in Figs. 2–4.

Results displayed in Figs. 2a, 2b, and 2c are for inlet Mach numbers of 0.1, 0.3, and 7, respectively. In these plots, two sets of results generated over a uniform grid of size 79 control volumes are compared against the exact analytical solution. The first set is obtained using the third-order SMART scheme [2] for all variables except density (for which the upwind [21] scheme is used). In the second set however, the SMART scheme is used for all variables including density. Results shown in Fig. 2a ($M_{in} = 0.1$, subsonic throughout) indicate that the solution is nearly insensitive to using an HR scheme when interpolating for density. This is expected, since for this inlet Mach number value, variations in density are small and the flow can be considered to be nearly incompressible.

For $M_{in} = 0.3$ (Fig. 2b), the backpressure is chosen such that a supersonic flow is obtained in the diverging section (i.e., $M_{th} = 1$, transonic). The Mach number distributions after the throat are depicted in Fig. 2b. As shown, the use of an HR scheme for interpolating the values of density at the control volume faces improves predictions. In fact, displayed results reveal that the profile predicted with values of density at the control volume faces calculated using an HR scheme is nearly coincident with the exact solution. The Mach number distributions depicted in Fig. 2c are for a fully supersonic flow in the nozzle. The trend of results is similar

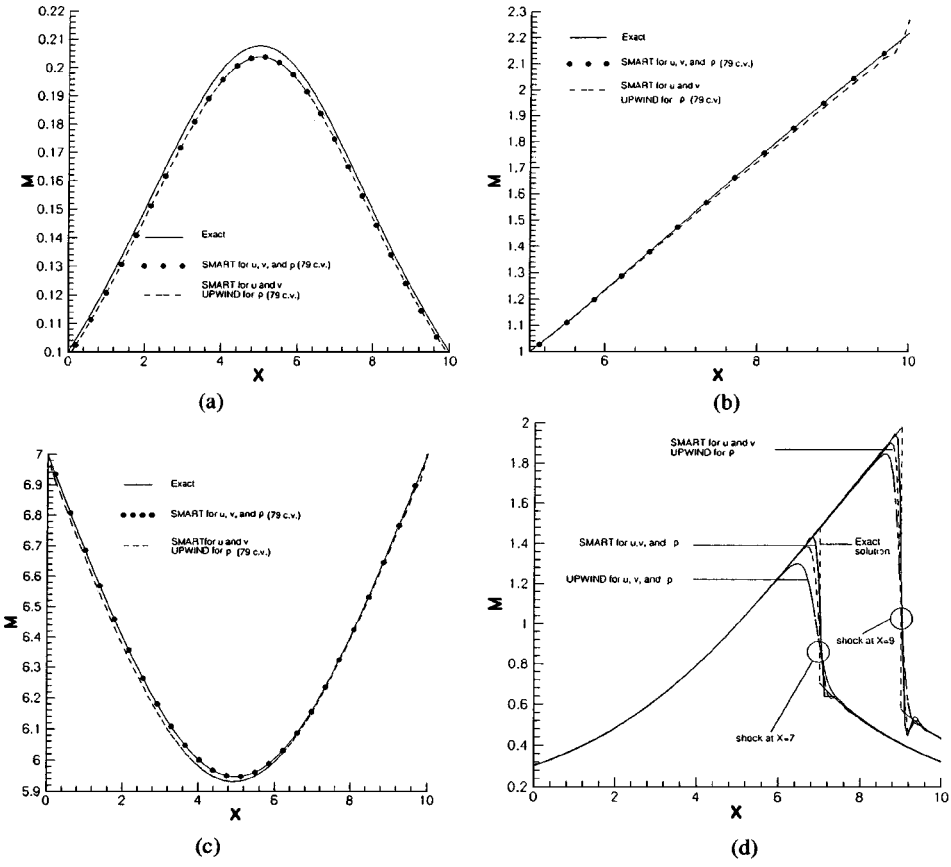

FIG. 2. Comparison of Mach number variation for an inlet Mach number of value (a) 0.1 (subsonic), (b) 0.3 (transonic), (c) 7 (supersonic), and (d) 0.3 (transonic with normal shock waves at $X = 7$ or $X = 9$).

to that of Fig. 2b. Again, important improvements are obtained when using the SMART scheme for density interpolation.

The accuracy of the new technique in predicting normal shock waves is revealed by the Mach number distributions displayed in Fig. 2d. Two backpressure values that cause normal shock waves at $x = 7$ and $x = 9$ are used. For each backpressure, three different solutions (one using the upwind scheme for all variables, the second one using the SMART scheme for all variables, the third one using the SMART scheme for all variables except density for which the upwind scheme is used) are obtained and compared against the exact solution. All solutions are obtained by subdividing the domain into 121 uniform control volumes. As shown, predictions obtained using the upwind scheme for all variables are very smooth but highly diffusive and cause a smearing in the shock wave.

Results obtained using the SMART scheme for all variables except density are more accurate than those obtained with the upwind scheme and cause less smearing in the shock waves. The best results are, however, obtained when employing the SMART scheme for all variables including density. The plots also reveal that solutions obtained using the SMART scheme show some oscillations behind the shock. This is a feature of all HR schemes. The oscillations are usually centered on the accurate solution and are reduced with grid refinement in both wavelength and amplitude [28].

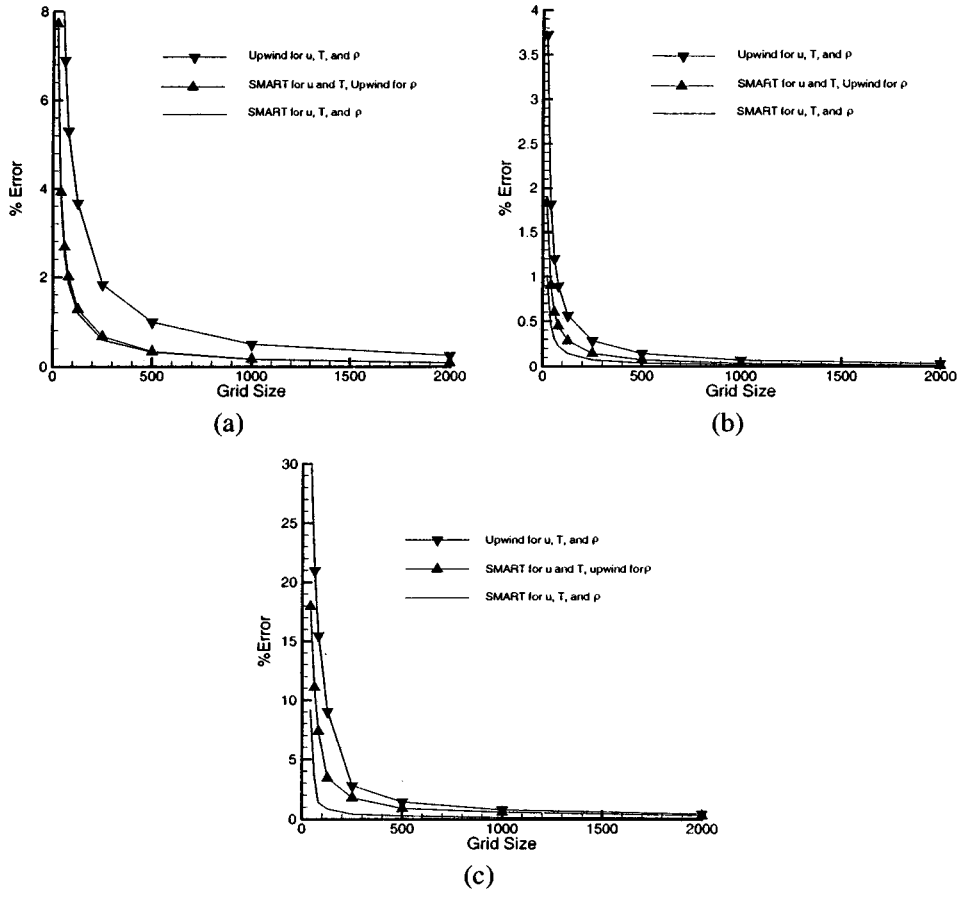

FIG. 3. Comparison of % error in the solution of one-dimensional (a) subsonic ($M_{in} = 0.1$), (b) supersonic ($M_{in} = 7$), and (c) transonic ($M_{in} = 0.3$ with a normal shock wave at $x = 7$) nozzle flow.

To highlight the performance characteristics of the new density treatment in the pressure-based method, a series of solutions for some of the above-mentioned cases was generated using different grid sizes. A summary of error norms versus the number of grid points used is presented in Fig. 3. Figures 3a and 3b are for inlet Mach numbers of 0.1 and 7, respectively. Figure 3c, however, is for an inlet Mach number of 0.3 with a normal shock wave at $x = 7$. The number of grid points was varied from 21 to 2000. Since an exact analytical solution is available, the error was defined as

$$\%\text{Error} = \underset{i=1}{\overset{N}{\text{MAX}}} \left\{ 100 \frac{|\phi_{\text{exact}} - \phi_{\text{computed}}|}{\phi_{\text{exact}}} \right\}. \tag{22}$$

The trend of results is similar to that discussed above with the percent error generally decreasing with increasing the grid density. The virtues of using an HR scheme for computing interface density values are more pronounced at high Mach numbers (Figs. 3b and 3c). In all cases, the worst solution is obtained when using the upwind scheme for all variables, and the best one is attained when utilizing the HR SMART scheme for all variables. As depicted in Fig. 3, the improvement when using an HR scheme for density decreases with increasing the number of grid points. This is expected since all approximations should converge to the

exact solution as the grid size approaches infinity (Fig. 3). Moreover, it may be of interest to mention that the optimum value of the under-relaxation factor increases with increasing both the grid density and the inlet Mach number. For the results presented in Fig. 3, the under-relaxation factors for the various variables varied from a minimum of 0.2 for the grid of size 21 to 0.8 for the grid of size 2000. This increase is attributed to a better solution at the beginning of the iterative process, as a result of using a larger number of grid points. The value 0.2 could be increased during the iterative process after a relatively good solution has been established. The need for a small under-relaxation factor at low Mach numbers is attributed to the large pressure correction values that result at the beginning of the iterative process and which are used to correct the density. Since at low Mach number density variations are small, high under-relaxation is needed. Definitely, the under-relaxation values may be increased after obtaining relatively good estimates. Moreover, the number of iterations needed to obtain a converged solution increases with increasing the number of grid points. The required number of iterations to obtain a converged solution (residuals for this one-dimensional problem were driven to machine error), for the cases presented in Fig. 3, varied from 1000 (for the grid of size 21) to 20,000 iterations when using 2000 grid points. These values may not be the optimum ones because of the large number of parameters involved. For example, under-relaxing the interface ϕ values (including density) may accelerate the convergence rate. All results presented in this paper were obtained without adopting such a practice. Furthermore, when using an HR scheme for all variables including density, the number of iterations needed to achieve a certain level of accuracy is nearly the same as the one needed when using an HR scheme for all variables excluding density (for which the upwind scheme is used).

To justify the above statements, additional runs for the subsonic ($M_{in} = 0.1$) and supersonic ($M_{in} = 7$) cases were performed. In these runs, the grid density was varied from 21 to 2000, and predictions were obtained using the various schemes. Computations were stopped when the maximum residual over all control volumes and for all variables dropped below 10^{-8}. The same initial guess for a given grid was used with all schemes. All variables were assigned the same under-relaxation factor value. The number of TDMA sweeps for all variables was set to 1. The under-relaxation factors used and numbers of iterations required by the various schemes are summarized in Table Ia for the subsonic flow and Table Ib for the supersonic flow. These values were obtained after a series of exploratory runs and were found to minimize the number of iterations within the above set constraints.

In the subsonic case (Table Ia), it was not possible to start the iteration process over relatively coarse grids ($\leq$101) with a high value of the under-relaxation factor. For these cases, two values are reported. The first one corresponds to the under-relaxation factor needed to prevent divergence at the beginning of the iterations. With this value held constant throughout the computations, the number of iterations needed are as shown in the first three rows of Table Ia. These numbers can be greatly reduced, as mentioned earlier, by gradually increasing the value of the under-relaxation factor from the starting value to a maximum of 0.95. For dense grids ($\geq$201), the value of 0.95 can be used throughout the computations. As can be seen, increasing the under-relaxation factor reduces the number of iterations, on average, by a factor of 5. Furthermore, for this case, the number of iterations required by the upwind scheme is only 9% lower for the coarsest grid used and decreases with increasing grid density until for the finest grid, it becomes equal to the one needed by other schemes. Moreover, the number of iterations required when using the SMART scheme for all variables including density is nearly equal to the one required when using the SMART scheme for all

TABLE I(a)
Under-Relaxation Factors and Number of Iterations Needed for the Subsonic Flow in a Converging–Diverging Nozzle (M_{in} = 0.1)

	All Upwind		All SMART		Upwind for ρ, SMART for u and T	
Grid	Under-relaxation	Number of iterations	Under-relaxation	Number of iterations	Under-relaxation	Number of iterations
21	0.25	2513	0.25	2887	0.25	2883
51	0.4	3242	0.4	4045	0.4	4021
101	0.55	4052	0.55	4446	0.55	4432
21	0.25–0.95	643	0.25–0.95	703	0.25–0.95	694
51	0.4–0.95	636	0.4–0.95	755	0.4–0.95	747
101	0.55–0.95	624	0.55–0.95	714	0.55–0.95	703
251	0.95	851	0.95	894	0.95	873
501	0.95	1562	0.95	1583	0.95	1581
2000	0.95	5703	0.95	5705	0.95	5705

variables excluding density for which the upwind scheme is used. Furthermore, the number of iterations generally increases with increasing grid density.

For the supersonic flow, the under-relaxation factors and number of iterations needed are depicted in Table Ib. With the upwind scheme, it was possible to obtain converged solutions over all grid sizes with an under-relaxation factor of value 0.95. However, it was not possible with the SMART scheme to use a value higher than 0.6. This has resulted in a noticeably lower number of iterations for the upwind scheme. Nevertheless, the number of iterations required when using the SMART scheme for all variables including density is still very close to the one needed when using the SMART scheme for all variables, excluding density, for which the upwind scheme is used.

As a further check on the applicability of the new technique in the subsonic, transonic, and supersonic regimes, results are generated for several inlet Mach number values $0.1 \leq M_{in} \leq 7$ and displayed in Fig. 4a. As shown, the Mach number distributions are in excellent agreement with the exact solution. Moreover, two-dimensional predictions for some of the

TABLE I(b)
Under-Relaxation Factors and Number of Iterations Needed for the Supersonic Flow in a Converging–Diverging Nozzle (M_{in} = 7)

	All Upwind		All SMART		Upwind for ρ, SMART for u and T	
Grid	Under-relaxation	Number of iterations	Under-relaxation	Number of iterations	Under-relaxation	Number of iterations
21	0.95	34	0.6	130	0.6	110
51	0.95	42	0.6	140	0.6	140
101	0.95	51	0.6	202	0.6	206
251	0.95	73	0.6	383	0.6	390
501	0.95	103	0.6	672	0.6	678
2000	0.95	253	0.6	2269	0.6	2275

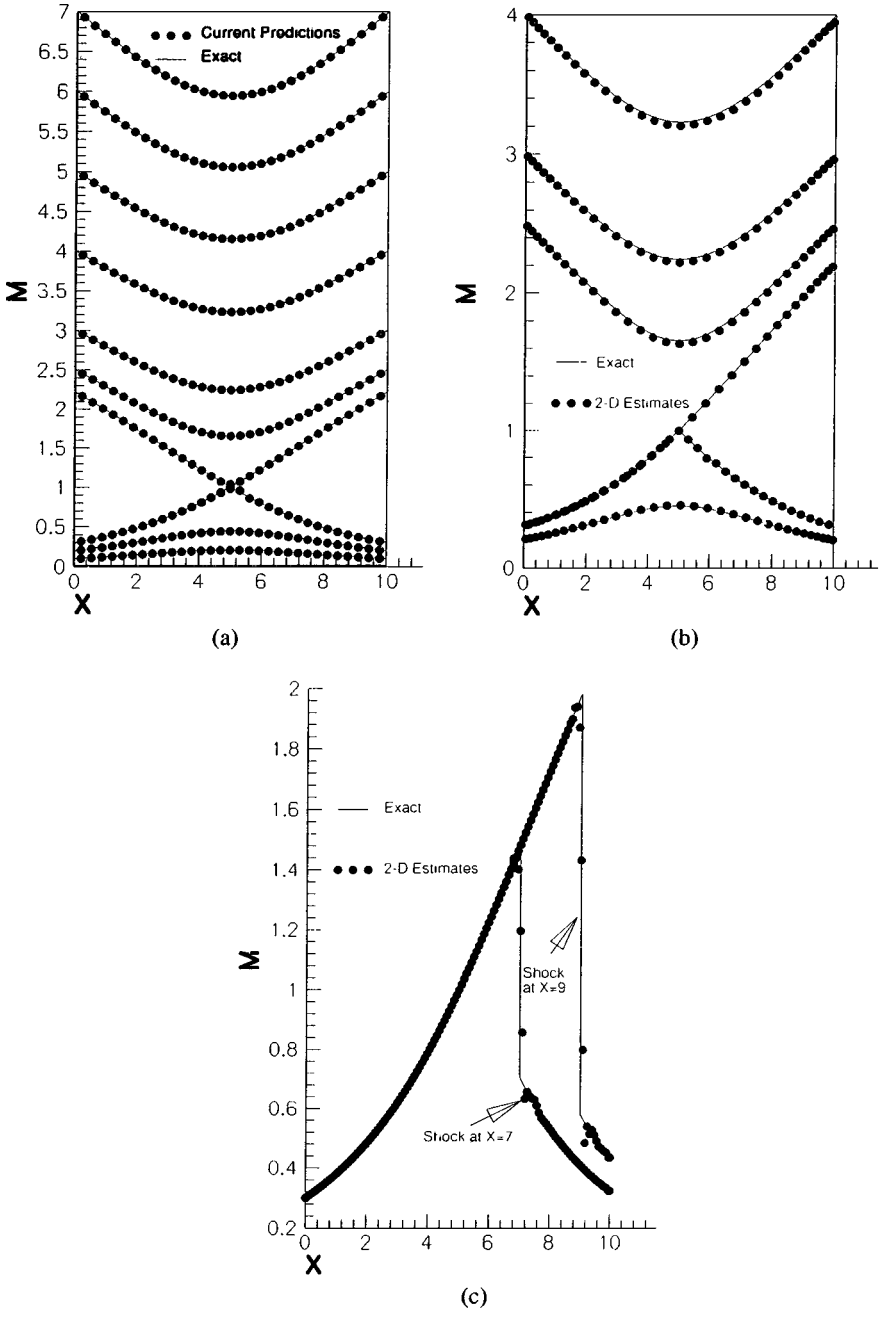

FIG. 4. (a) Comparison of Mach number distributions for one-dimensional inviscid nozzle flow. (b) Comparison of area-averaged Mach number distributions for inviscid nozzle flow from two-dimensional solutions. (c) Comparison of area-averaged Mach number distributions for inviscid nozzle flow with normal shock waves from two-dimensional solutions.

above-presented cases were generated with 100×15 mesh covering one half of the nozzle. The resultant area-averaged variations of Mach number are depicted in Figs. 4b and 4c. Results were obtained using the SMART scheme for all variables including density. As for the quasi-one-dimensional predictions, results are in excellent agreement with the exact solutions.

Flow over a Circular Arc Bump

The physical situation consists of a channel of width equal to the length of the circular arc bump and of total length equal to three lengths of the bump. This problem has been used by many researchers [30, 31, 35, 36] to test the accuracy and stability of numerical algorithms. Results are presented for three different types of flow (subsonic, transonic, and supersonic). For subsonic and transonic calculations, the thickness-to-chord ratio is 10%, and for supersonic flow calculations it is 4%. In all flow regimes, predictions obtained over a relatively coarse grid using the SMART scheme for all variables including density are compared against results obtained over the same grid using the SMART scheme for all variables except density, for which the UPWIND scheme is used. Because of the unavailability of an exact solution to the problem, a solution using a dense grid is generated and treated as the most accurate solution against which coarse grid results are compared.

Subsonic flow over a circular arc bump. With an inlet Mach number of 0.5, the inviscid flow in the channel is fully subsonic and symmetric across the middle of the bump. At the inlet, the flow is assumed to have uniform properties and all variables, except pressure, are specified. At the outlet section, the pressure is prescribed and all other variables are extrapolated from the interior of the domain. The flow tangency condition is applied at the walls. As shown in Fig. 5a, the physical domain is nonuniformly decomposed into 63×16 control volumes. The dense grid solution is obtained over a mesh of size 252×54 control volumes. Isobars displayed in Fig. 5b reveal that the coarse grid solution obtained with the SMART scheme for all variables falls on top of the dense grid solution. The use of the upwind scheme for density, however, lowers the overall solution accuracy. The same conclusion can be drawn when comparing the Mach number distribution along the lower and upper walls of the channel. As seen in Fig. 5c, the coarse grid profile obtained using the SMART scheme for density is closer to the dense grid profile than the one predicted employing the upwind scheme for density. The difference in results between the coarse grid solutions is not large for this test case. This is expected since the flow is subsonic, and variations in density are relatively small. Larger differences are anticipated in the transonic and supersonic regimes.

Transonic flow over a circular arc bump. With the exception of the inlet Mach number being set to 0.675, the grid distribution and the implementation of boundary conditions are identical to those described for subsonic flow. Results are displayed in Fig. 6 in terms of isobars and Mach profiles along the walls. In Fig. 6a isobars generated using a dense grid and the SMART scheme for all variables are displayed. Figure 6b presents a comparison between the coarse grid and dense grid results. As shown, the use of the HR SMART scheme for density greatly improves the predictions. Isobars generated over a coarse grid (63×16 control volumes (c.v.)) using the SMART scheme for all variables are very close to those obtained with a dense grid (252×54 c.v.). This is different than coarse grid results obtained using the upwind scheme for density and the SMART scheme for all other variables, which

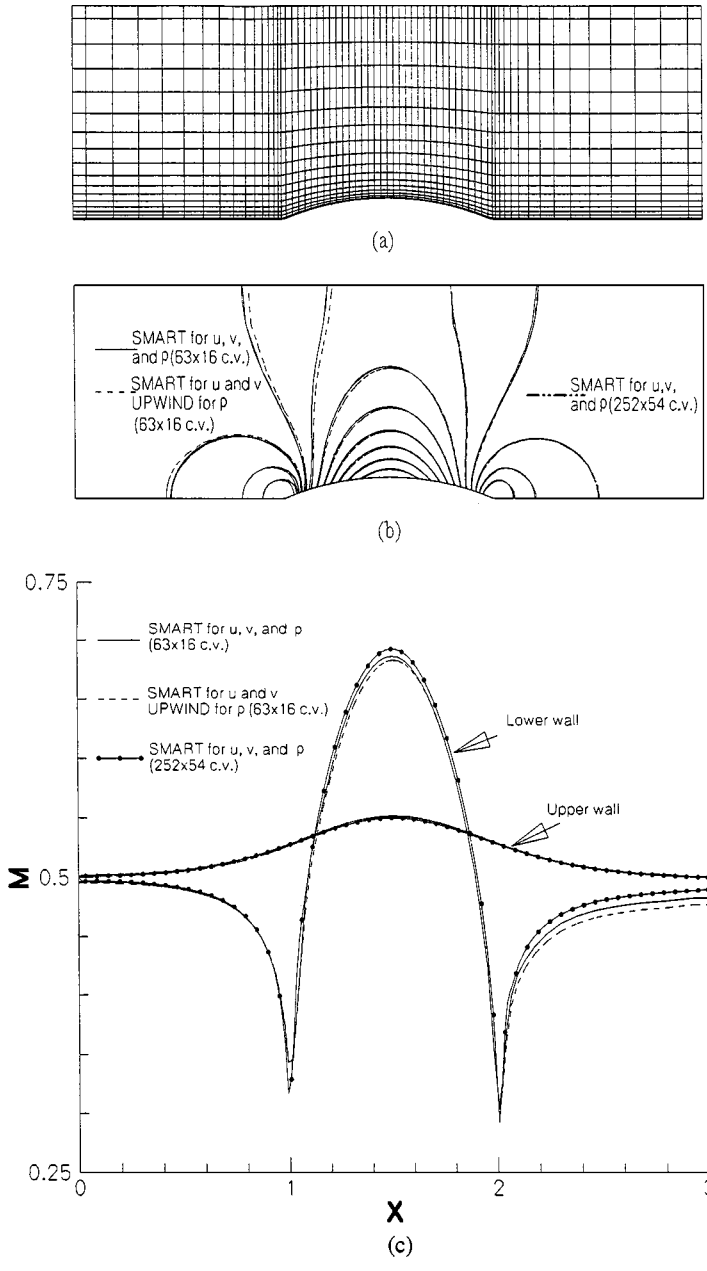

FIG. 5. Subsonic flow over a 10% circular bump; (a) coarse grid used, (b) isobars, and (c) profiles along the walls.

noticeably deviate from the dense grid solution. This is further apparent in Fig. 6c where Mach number profiles along the lower and upper walls are compared. As shown, the most accurate coarse grid results are those obtained with the SMART scheme for all variables, and the worst results are achieved with the upwind scheme for all variables. The maximum Mach number along the lower wall ($\cong$1.41), predicted with a dense grid, is in excellent agreement with published values [30, 31, 35]. The use of an HR scheme for density greatly enhances the solution accuracy, with coarse grid profiles generated using the SMART scheme for

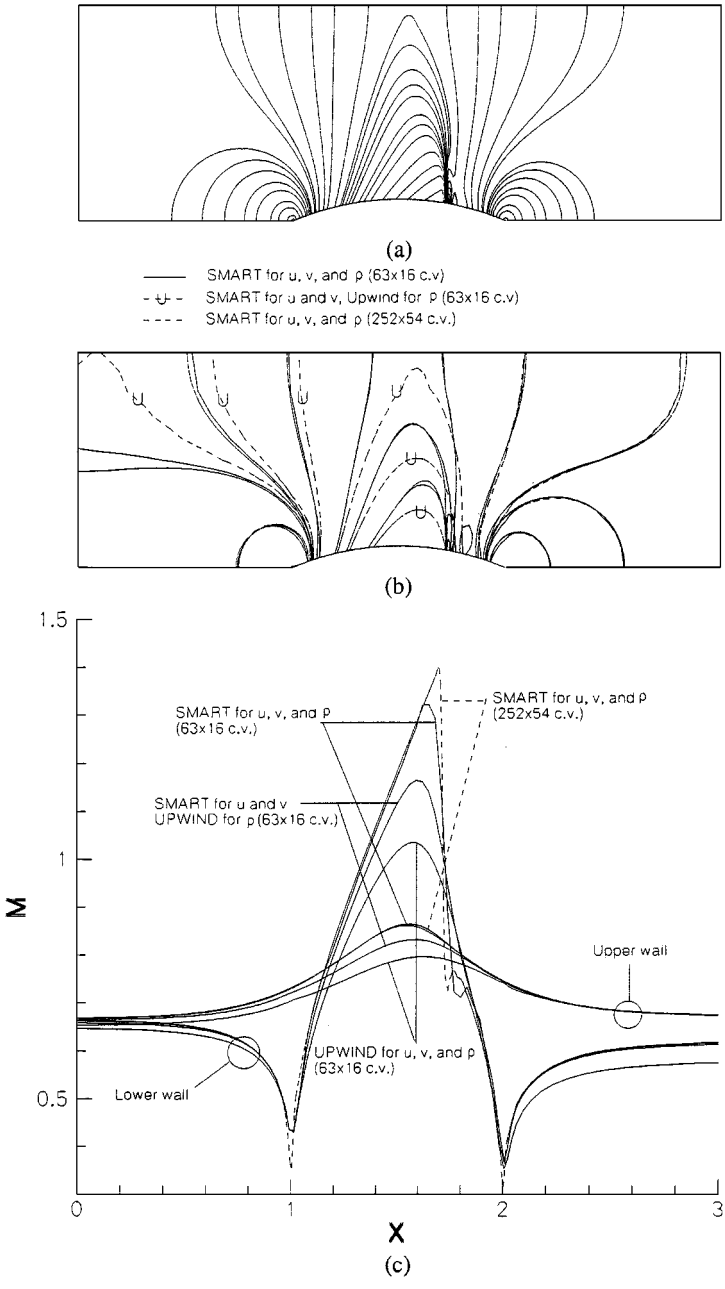

FIG. 6. Transonic flow over a 10% circular bump; (a) isobars using a dense grid, (b) isobars using various schemes, and (c) profiles along the walls.

all variables being very close to the dense grid results. By comparing coarse grid profiles along the lower wall, the all-SMART solution is about 11% more accurate than the solution obtained using SMART for all variables and upwind for density and 21% more accurate than the highly diffusive all-upwind solution.

Supersonic flow over a circular arc bump. Computations are presented for two inlet Mach number values of 1.4 and 1.65. For these values of inlet Mach number and for the

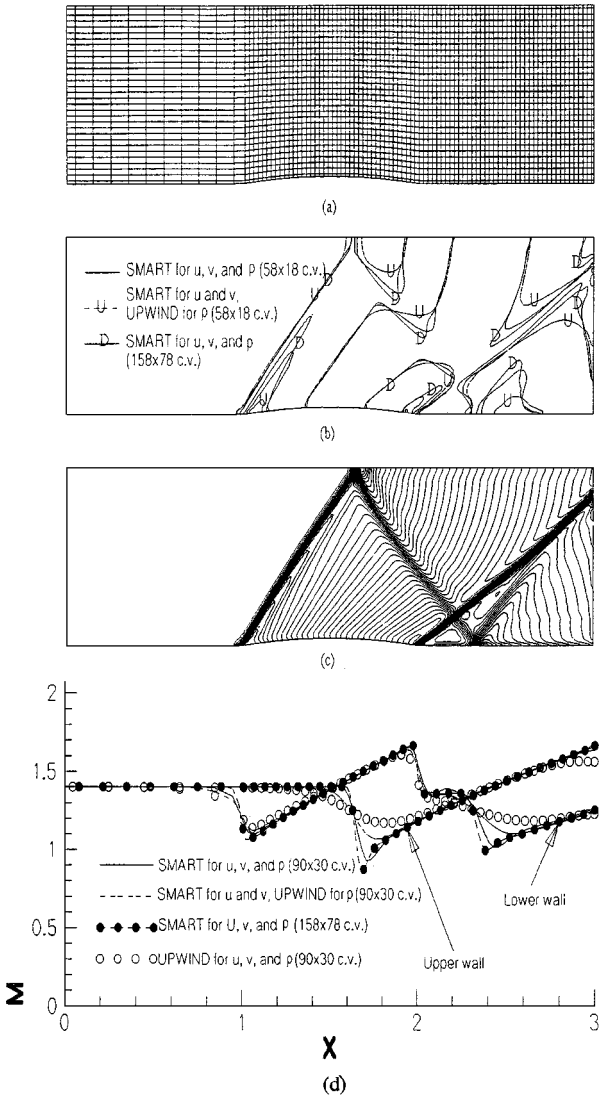

FIG. 7. Supersonic flow over a 4% circular bump ($M_{in} = 1.4$); (a) coarse grid used, (b) Mach number contours using various schemes, (c) Mach number contours using a dense grid, and (d) profiles along the walls.

used geometry, the flow is also supersonic at the outlet. Thus, all variables at inlet are prescribed, and at outlet all variables are extrapolated. For $M_{in} = 1.4$, results are presented in Figs. 7 and 8. The coarse grid used is displayed in Fig. 7a. Mach number contours are compared in Fig. 7b. As before, the coarse grid all-SMART results (58×18 c.v.), being closer to the dense grid results (158×78 c.v.), are more accurate than those obtained when using the upwind scheme for density. The fine grid Mach contours are displayed in Fig. 7c. As depicted, the reflection and intersection of the shocks is very well resolved without undue oscillations. The Mach profiles along the lower and upper walls, depicted in Fig. 7d, are in excellent agreement with published results [61] and reveal good enhancement in accuracy when using the SMART scheme for evaluating interface density values. The use of the upwind scheme to compute density deteriorates the solution accuracy even though an

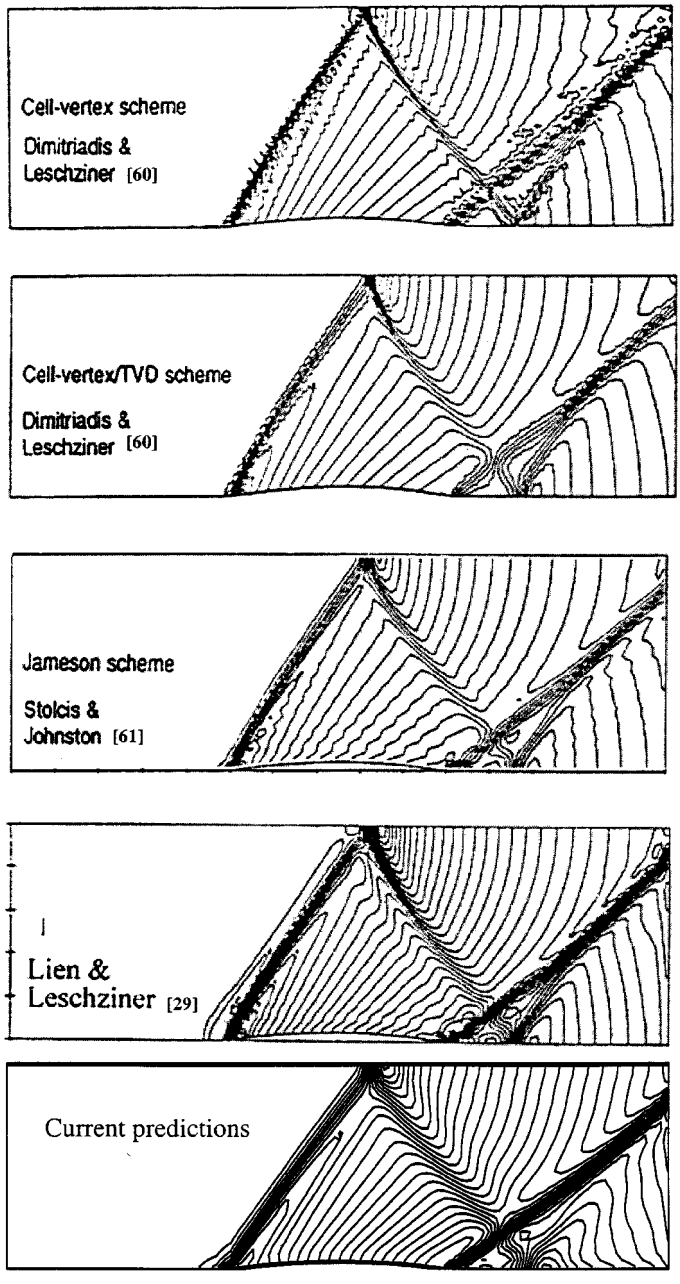

FIG. 8. Supersonic inviscid flow over 4% bump ($M_{in} = 1.4$): Mach-number contours.

HR scheme is used for other variables. The all-upwind results are highly diffusive. Finally, results for this case were obtained over a grid of 90×30 nodes, of which 80×30 were uniformly distributed in the region downstream of the bump's leading corner. Resulting Mach contours are compared in Fig. 8 with four other solutions [31, 62, 63] using the same grid density. The comparison demonstrates the credibility and superiority of the current solution methodology. The wiggles and oscillations in some regions around the shock waves in the published solutions are not present in the newly predicted one.

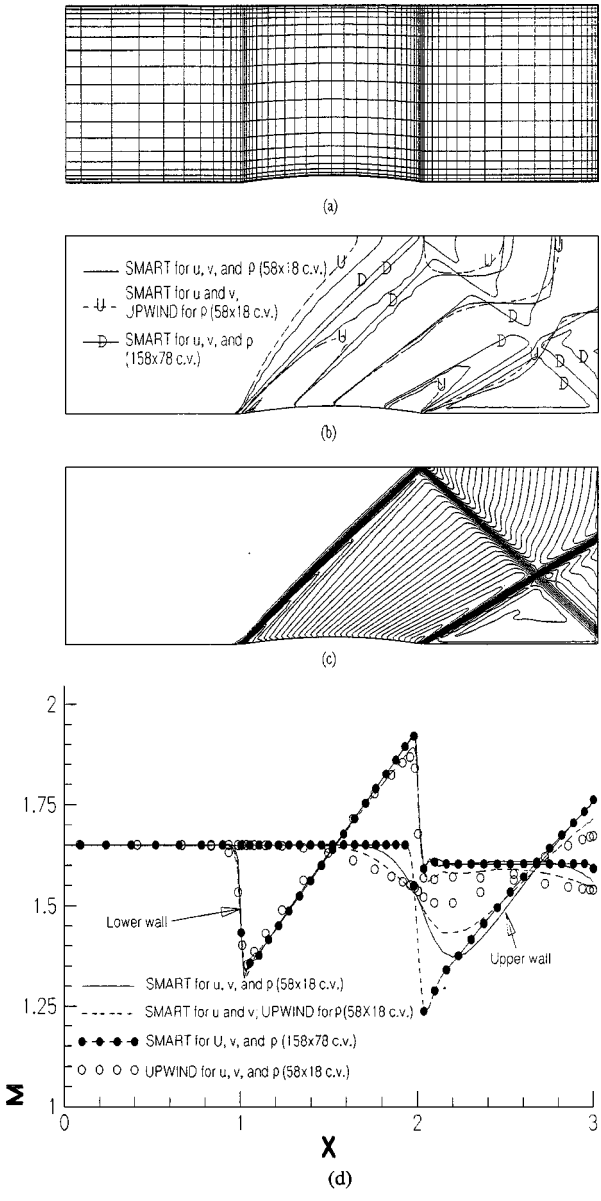

FIG. 9. Supersonic flow over a 4% circular bump ($M_{in} = 1.65$); (a) coarse grid used, (b) Mach number contours using various schemes, (c) Mach number contours using a dense grid, and (d) profiles along the walls.

For $M_{in} = 1.65$, results are depicted in Fig. 9. The coarse grid used is shown in Fig. 9a, and the Mach contours are compared in Fig. 9b. The trend of results is consistent with what was obtained earlier. Fine grid results displayed in Figs. 9c and 9d are in excellent agreement with published results [30, 35]. The Mach contours in Fig. 9c are very smooth and do not show any sign of oscillations. The profiles along the lower and upper walls indicate once more that the use of an HR scheme for density increases the solution accuracy. Thus, for subsonic, transonic, and supersonic flows the use of an HR scheme for calculating interface density values increases the solution accuracy.

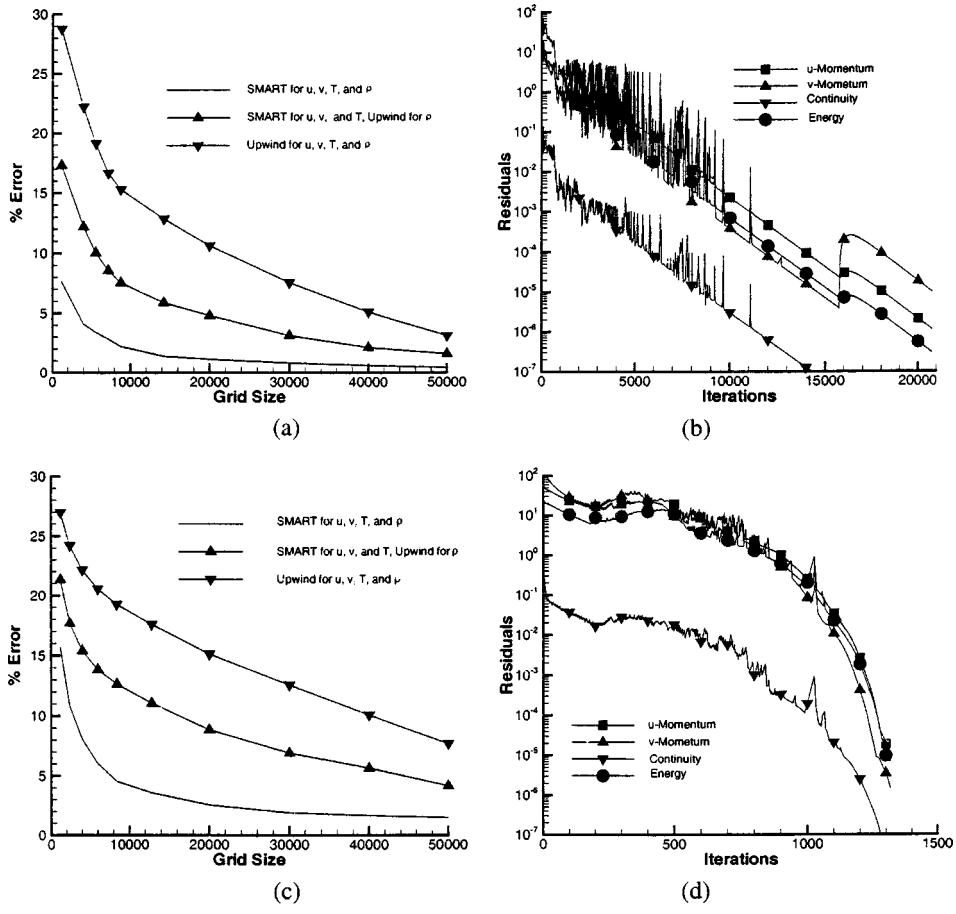

FIG. 10. (a) Comparison of % error and (b) convergence history for the transonic flow ($M_{in} = 0.675$) over a 10% circular bump. (c) Comparison of % error and (d) convergence history for the supersonic flow ($M_{in} = 1.65$) over a 4% circular bump.

Effect of grid size. As for the previous problem, the performance characteristics of the newly suggested method is studied by obtaining a series of solutions, using different grid sizes, for the transonic ($M_{in} = 0.675$) and supersonic ($M_{in} = 1.65$) cases. The variation of error with the grid size along with the convergence history is depicted in Fig. 10. The percent error in the solution was calculated using Eq. (22) with ϕ_{exact} because of the unavailability of an exact solution, replaced by a solution obtained over a fine mesh of size 360×270 grid points. As can be seen, the error decreases with increasing the grid size. By comparing plots in Figs. 10a and 10c, it is obvious that improvements in predictions are more pronounced for the supersonic case where changes in pressure have higher effects on density. In Figs. 10b and 10d, the convergence history for the solutions obtained using a grid of size 254×100 grid points is displayed. For reasons explained earlier, the two plots reveal the need for fewer iterations to obtain a converged solution in the supersonic case. It should be stressed that it is not the intention of this work to study the convergence characteristics of pressure-based methods. The algebraic equation solver used here is the line-by-line TDMA. The use of multigrid methods [64] or other solvers [65, 66] would definitely accelerate the rate of convergence. This may equally be true with preconditioning methods [15–22]. Nevertheless,

the virtues of using an HR scheme for evaluating interface density values are undoubtedly clear.

Supersonic Flow over a Step

The physical situation and boundary conditions for the problem are depicted in Fig. 11a. The problem was first solved using the upwind scheme, and the predicted isobars are depicted in Fig. 11b. In Fig. 11c, the isobars reported in [29] are presented. As shown, the current predictions fall on top of the ones reported by Marchi and Maliska [29], eliminating any doubts about the correctness of the implementation of the solution algorithm and boundary conditions. The isobars resulting from a dense grid solution (238×108 c.v.) using the upwind scheme for all variables are presented in Fig. 12a. The effectiveness of using an HR scheme for density is demonstrated through the comparison depicted in Fig. 12b. Two different isobars representing pressure ratios of values 0.9 and 2.5 are considered. Solutions obtained over a course grid (38×36 c.v.) using (i) the SMART schemes for all variables, (ii) the SMART scheme for all variables except density and the upwind scheme for density, and (iii) the upwind scheme for all variables are compared against a dense grid solution (238×108 c.v.) generated using the upwind scheme for all variables. Once more the virtues of using an HR scheme for density is obvious. The coarse grid isobars obtained using the SMART scheme for all variables, being nearly coincident with dense grid isobars, are remarkably more accurate than coarse grid results obtained using the SMART scheme for all variables except density and the upwind scheme for density.

Ideal Unsteady Duct Filling

Having established the credibility of the solution method, an unsteady process of duct filling is considered. This problem resembles the well-known shock tube problem recently used by Karimian and Schneider [67] and Darbandi and Schneider [68] in testing their pressure-based methods. The physical situation for the problem consists of a duct containing a gas ($\gamma = 1.4$) that is isentropically expanded from atmospheric pressure. The duct is considered to be frictionless, adiabatic, and of constant cross section. Moreover, it is assumed that the duct is opened instantaneously to the surrounding atmosphere, that inflow is isentropic, and that in the fully open state the effective flow area at the duct end is equal to the duct cross-sectional area. The unsteady one-dimensional duct filling process is solved using a two-dimensional code over a uniform grid of density 299×3 control volumes, a time step of value 10^{-4}, and the SMART scheme for all variables.

The problem is solved for a surrounding to duct pressure ratio of 2.45 and generated results are displayed in Fig. 13. Because of the lower pressure of the gas contained in the duct, when the duct end is suddenly opened, a compression wave is established instantly as a shock wave. The wave diagram for the process is shown in Fig. 13a. The shock wave moves in the duct until the closed end is reached. On reaching the closed end, the compression wave is reflected and the duct filling process continues until the reflected shock wave is at the open end. Beyond that, duct emtying starts and computations were stopped at that moment in time. In addition, the path of the first particle to enter the duct is shown in the figure. This was computed by storing the duct velocities at all time steps and then integrating in time to locate the position of the particle. Results depicted in Fig. 13a were compared against similar ones reported by Azoury [69] using a graphical method. The two sets of results were found to be in excellent agreement with the ones computed here, falling right on top of those reported.

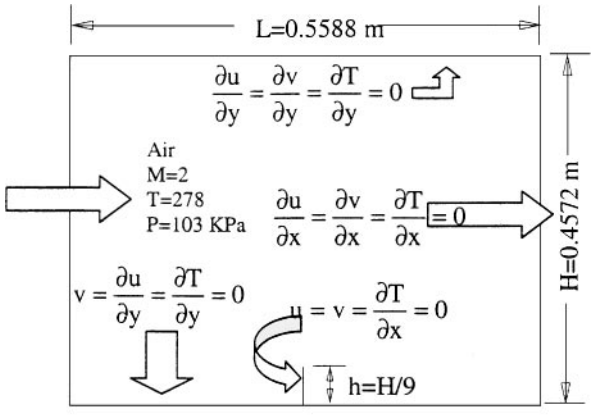

(a)

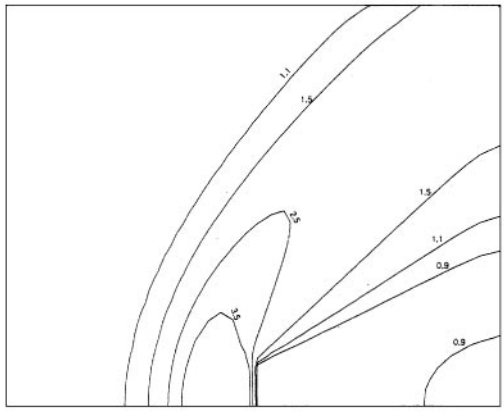

(b)

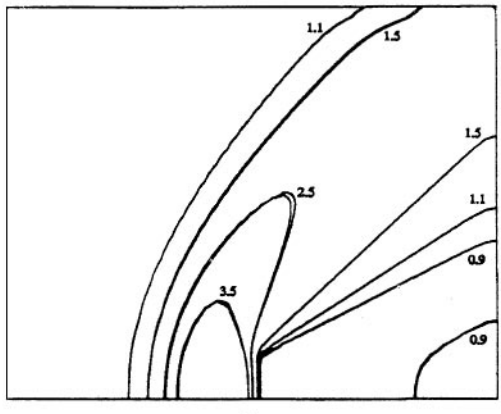

(c)

FIG. 11. Supersonic flow over an obstacle: (a) physical situation, (b) isobars using the upwind scheme (40×38 grid points), and (c) results obtained by Marchi and Maliska [29] using the upwind scheme (44×36 grid points).

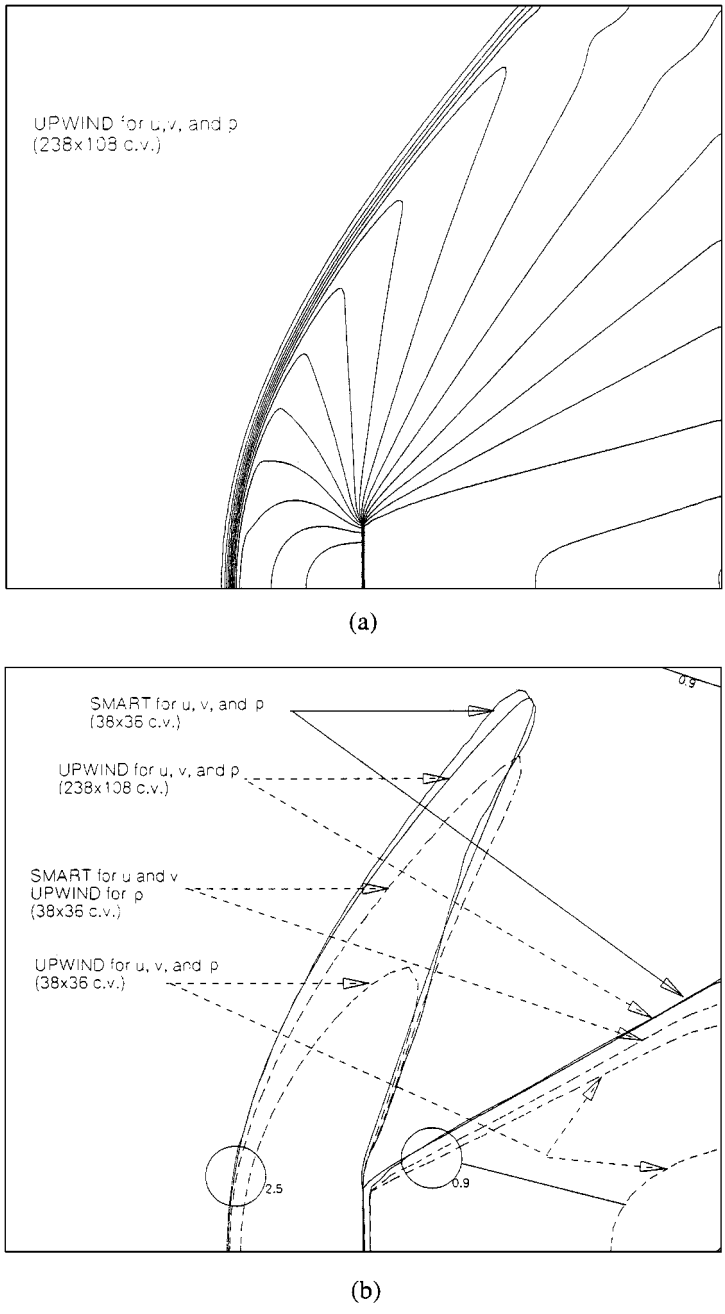

FIG. 12. Supersonic flow over an obstacle: (a) isobars generated using a dense grid; (b) isobars generated using different schemes.

The variation of Mach number with time at the open end of the duct is displayed in Fig. 13b. With the exception of the slight overshoot at the beginning of the computations, the Mach number remains constant throughout the filling process, and it instantaneously decreases to zero at the time when the reflected shock wave reaches the open end of the duct. When using the same reference quantities, the analytical solution to the problem reported in [69] predicts

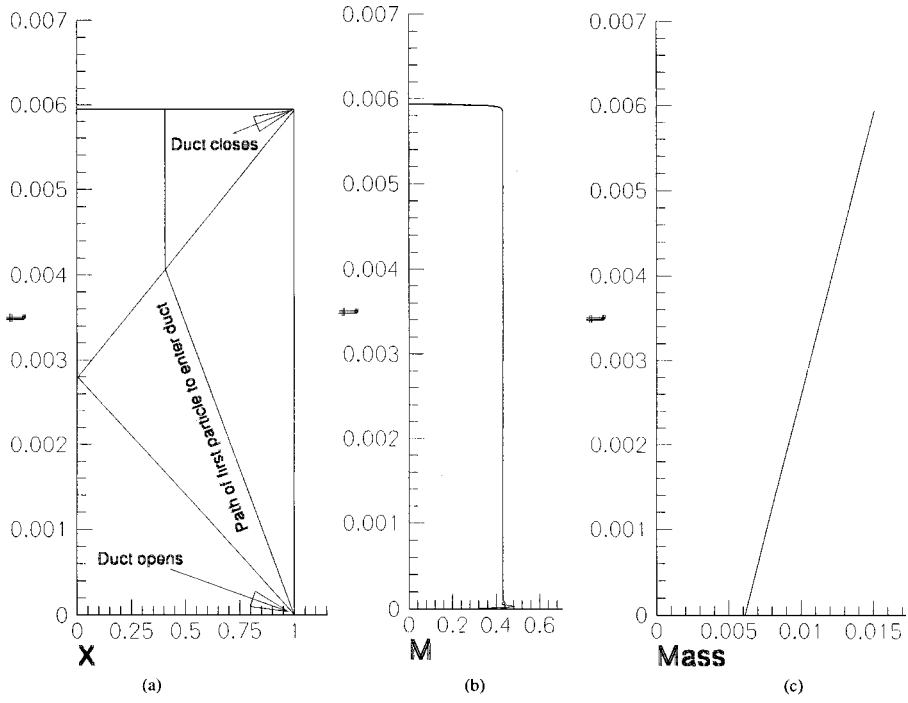

FIG. 13. (a) Wave diagram for optimum duct-filling process; (b) Mach number distribution at inflow; (c) variation of mass with time.

a constant Mach number of value 0.4391, which is 0.21% different than the one obtained here. Moreover, the instantaneous decrease of Mach number to zero is well predicted by the method. Finally, the increase in mass within the duct is presented in Fig. 13c. As expected, because of the constant value of the inlet Mach number, the mass increases linearly with time.

CONCLUDING REMARKS

A new collocated high-resolution pressure-based algorithm for the solution of fluid flow at all speeds was formulated. The new features in the algorithm include the use of an HR scheme in calculating the density values at the control volume faces and the use of the NVSF methodology for bounding the convection fluxes. The method was tested by solving four problems representing flow in a converging–diverging nozzle, flow over a bump, flow over an obstacle, and unsteady duct filling. Mach number values spanning the entire subsonic to supersonic spectrum, including transonic flows with strong normal shock waves, were considered. In all cases, results obtained were very promising and revealed good enhancement in accuracy at high-Mach-number values when calculating interface density values using a high-resolution scheme.

APPENDIX NOMENCLATURE

$a_P^\phi, a_E^\phi, .$	Coefficients in the discretized equation
b_P^ϕ	Source term in the discretized equation for ϕ
C_ρ	Coefficient equals to $1/RT$

$D[\phi]$	The D operator
$\mathbf{D}[\phi]$	The vector form of the D operator
F_f	Convective flux at cell face "f"
$H[\phi]$	The H operator
$\mathbf{H}[\phi]$	The vector form of the H operator
$\mathbf{i}$	Unit vector in the x-direction
$\mathbf{j}$	Unit vector in the y-direction
J_f^C	Total scalar flux across cell face "f" due to convection
J_f^D	Total scalar flux across cell face "f" due to diffusion
J_f	Total scalar flux across cell face "f"
M	Mach number
P	Pressure
Q^ϕ	Source term for ϕ
R	Gas constant
$\mathbf{S}_f$	Surface vector
T	Temperature
t	Time
u, v	Velocity components in the x- and y-directions
U_f	Interface flux velocity $(\mathbf{v}_f \cdot \mathbf{S}_f)$
$\mathbf{v}$	$u\mathbf{i} + v\mathbf{j}$
x, y	Cartesian coordinates

Greek Symbols

$\Delta[\phi]$	The Δ operator
Φ	Dissipation term in energy equation
Γ^ϕ	Diffusion coefficient for ϕ
Ω	Cell volume
β	Thermal expansion coefficient
δt	Time step
$\tilde{\phi}$	Normalized scalar variable
ϕ	Scalar variable
μ	Viscosity
ρ	Density

Subscripts

$e, w, \ldots$	Refers to the east, west, ... face of a control volume
$E, W, \ldots$	Refers to the East, West, ... neighbors of the main grid point
f	Refers to control volume face f
NB	Refers to neighbors of the P grid point
P	Refers to the P grid point

Superscripts

$^\circ$	Refers to values from the previous time step
(n)	Refers to value from the previous iteration
*	Refers to intermediate values at the current iteration
$'$	Refers to correction field

C Refers to convection contribution
D Refers to diffusion contribution
HR Refers to values based on an HR scheme
x Refers to component in x-direction
y Refers to component in y-direction
ϕ Refers to dependent variable

ACKNOWLEDGMENT

Thanks are due to Professor P. H. Azoury for reviewing the manuscript and for the valuable discussions the authors had with him during the various phases of the work.

REFERENCES

1. S. V. Patankar, *Numerical Heat Transfer and Fluid Flow* (Hemisphere, New York, 1981).
2. M. Darwish and F. Moukalled, A new route for building bounded skew-upwind schemes, Comput. Meth. *Appl. Mech. Eng.* **129**, 221 (1996).
3. F. Moukalled and M. Darwish, A new bounded skew central difference scheme, part I. formulation and testing, *Numer. Heat Transfer. B* **31**, 91 (1997).
4. F. Moukalled and M. Darwish, A new family of streamline-based very high resolution schemes, *Numer. Heat Transfer*. **32**, 299 (1997).
5. M. Darwish and F. Moukalled, An efficient very high-resolution scheme based on an adaptive-scheme strategy, *Numer. Heat Transfer. B* **34**, 191 (1998).
6. F. Moukalled and M. Darwish, New family of adaptive very high resolution schemes, *Numer. Heat Transfer. B* **34**, 215 (1998).
7. J. Zhu and W. Rodi, A low dispersion and bounded convection scheme, *Comput. Meth. Appl. Mech. Eng*. **92**, 897 (1991).
8. P. H. Gaskell and A. K. C. Lau, Curvature compensated convective transport: SMART, a new boundedness preserving transport algorithm, *Int. J. Numer. Meth. Fluids* **8**, 617 (1988).
9. J. Zhu, A low-diffusive and oscillation-free convection scheme, *Comm. Appl. Numer. Meth*. **7**, 225 (1991).
10. H. Lin and C. C. Chieng, Characteristic-based flux limiters of an essentially third-order flux-splitting method for hyperbolic conservation laws, *Int. J. Numer. Meth. Fluids*. **13**, 287 (1991).
11. M. S. Darwish, A new high-resolution scheme based on the normalized variable formulation, *Numer. Heat Transfer B: Fundamentals* **24**, 353 (1993).
12. K. C. Karki, A calculation procedure for viscous flows at all speeds in complex geometries, Ph.D. thesis (University of Minnesota, 1986).
13. A. Rizzi and L. E. Eriksson, Computation of inviscid incompressible flow with rotation, *J. Fluid Mech.* **153**, 275 (1985).
14. D. Choi and C. L. Merkle, Application of time-iterative schemes to incompressible flow, *AIAA J*. **23**, 1518 (1985).
15. E. Turkel, Preconditioning methods for solving the incompressible and low speed compressible equations, *J. Comput. Phys*. **72**, 277 (1987).
16. Y. H. Choi and C. L. Merkle, The application of preconditioning to viscous flows, *J. Comput. Phys*. **105**, 207–223 (1993).
17. E. Turkel, V. N. Vatsa, and R. Radespiel, *Preconditioning Methods for Low Speed Flows*, Technical Paper 96-2460 (AIAA Press, Washington, DC, 1996).
18. D. L. Tweedt, R. V. Chima, and E. Turkel, *Preconditioning for Numerical Simulation of Low Mach Number Three-Dimensional Viscous Turbomachinary Flows*, Technical Paper 97-1828 (AIAA Press, Washington, DC, 1997).

19. B. Van Leer, W. T. Lee, and P. Roe, *Characteristic Time-Stepping or Real Preconditioning of the Euler Equations*, Technical Paper 91-1552 (AIAA Press, Washington, DC, 1991).
20. J. M. Weiss and W. A. Simith, Preconditioning applied to variable and constant density flows, *AIAA J*. **33**(11), 2050 (1995).
21. C. L. Merkle, J. Y. Sullivan, P. E. O. Buelow, and S. Venkateswaran, Computation of flows with arbitrary equations of state, *AIAA J*. **36**(4), 515 (1998).
22. J. R. Edwards and M. S. Liou, Low-diffusion flux-splitting methods for flows at all speeds, *AIAA J*. **36**(9), 1610 (1998).
23. E. Turkel, Preconditioning techniques in computational fluid dynamics, *Annu. Rev. Fluid Mech*. **31**, 385 (1999).
24. E. Turkel, A review of preconditioning methods for fluid dynamics, *Appl. Numer. Math.* **12**, 257 (1993).
25. W. Shyy and M. E. Braaten, *Adaptive grid Computation for Inviscid Compressible Flows Using a Pressure Correction Method*, Technical Paper 88-3566-CP (AIAA Press, Washington, DC, 1988).
26. W. Shyy and M. H. Chen, Pressure-based multigrid algorithm for flow at all speeds, *AIAA J*. **30**(11), 2660 (1992).
27. C. M. Rhie, *A Pressure Based Navier–Stokes Solver Using the Multigrid Method*, Technical Paper 86-0207 (AIAA Press, Washington, DC, 1986).
28. H. Q. Yang, S. D. Habchi, and A. J. Przekwas, General strong conservation formulation of Navier–Stokes equations in non-orthogonal curvilinear coordinates, *AIAA J*. **32**(5), 936 (1994).
29. C. H. Marchi and C. R. Maliska, A non-orthogonal finite-volume methods for the solution of all speed flows using co-located variables, *Numer. Heat Transfer B* **26**, 293 (1994).
30. I. Demirdzic, Z. Lilek, and M. Peric, A Collocated finite volume method for predicting flows at all speeds, *Int. J. Numer. Meth. Fluids* **16**, 1029 (1993).
31. F. S. Lien and M. A. Leschziner, A pressure-velocity solution strategy for compressible flow and its application to shock/boundary-layer interaction using second-moment turbulence closure, *J. Fluids Eng*. **115**, 717 (1993).
32. F. S. Lien and M. A. Leschziner, A general non-orthogonal collocated finite volume algorithm for turbulent flow at all speeds incorporating second-moment turbulence-transport closure, part 1: Computational implementation, *Comput. Meth. Appl. Mech. Eng.* **114**, 123 (1994).
33. E. S. Politis and K. C. Giannakoglou, A pressure-based algorithm for high-speed turbomachinery flows, *Int. J. Numer. Meth. Fluids* **25**, 63 (1997).
34. K. H. Chen and R. H. Pletcher, Primitive variable, strongly implicit calculation procedure for viscous flows at all speeds, *AIAA J*. **29**(8), 1241 (1991).
35. R. I. Issa and M. H. Javareshkian, Pressure-based compressible calculation method utilizing total varaiation diminishing schemes, *AIAA J*. **36**(9) 1652–1657 (1998).
36. S. M. H. Karimian and G. E. Schneider, Pressure-based control-volume finite element method for flow at all speeds, *AIAA J*. **33**(9), 1611 (1995).
37. G. E. Schneider and S. M. H. Kaimian, Advances in control-volume-based finite-element methods for compressible flows, *Comput. Mech*. **14**(5), 431 (1994).
38. S. M. H. Karimian and G. E. Schneider, Pressure-based computational method for compressible and incompressible flows, *AIAA J. Thermophys. Heat Trans.* **8**(2), 267 (1994).
39. M. Darbandi and G. E. Shneider, Momentum variable procedure for solving compressible and incompressible flows, *AIAA J*. **35**(12), 1801 (1997).
40. M. Darbandi and G. E. Schneider, *Use of a Flow Analogy in Solving Compressible and Incompressible Flows*, Technical Paper 97-2359 (AIAA Press, Washington, DC, 1997).
41. B. P. Leonard, Locally Modified quick scheme for highly convective 2-D and 3-D flows, in *Numerical Methods in Laminar and Turbulent Flows*, edited by C. Taylor and K. Morgan (Pineridge, Swansea, 1987, Vol. 15, pp. 35–47.
42. M. S. Darwish and F. Moukalled, Normalized variable and space formulation methodology for high-resolution schemes, *Numer. Heat Transfer B* **26**, 79 (1994).
43. A. Harten, High resolution schemes for hyperbolic conservation laws, *J. Comput. Phys*. **49**, 357 (1983).

44. P. J. Zwart, G. D. Raithby, and M. J. Raw, An integrated space–time finite-volume method for moving-boundary problems, *Numer. Heat Transfer B* **34**, 257 (1998).
45. L. H. Thomas, Elliptic Problems in Linear Difference Equations over a Network, Watson Science Computer Laboratory Report (Columbia University, New York, —.
46. S. T. Zalesak, Fully multidimensional flux-corrected transport algorithm for fluids, *J. Comput. Phys.* **31**, 335 (1979).
47. M. Chapman, FRAM nonlinear damping algorithm for the continuity equation, *J. Comput. Phys*. **44**, 84 (1981).
48. M. Peric, *A Finite Volume Method for the Prediction of Three Dimensional Fluid Flow in Complex Ducts*, Ph.D. thesis (Imperial College, Mechanical Engineering Department, London, 1985).
49. J. Zhu and M. A. Leschziner, A local oscillation-damping algorithm for higher order convection schemes, *Comput. Meth. Appl. Mech. Eng*. **67**, 355 (1988).
50. B. P. Leonard, Simple high-accuracy resolution program for convective modelling of discontinuities, *Int. J. Numer. Meth. Eng*. **8**, 1291 (1988).
51. S. V. Patankar and D. B. Spalding, A calculation procedure for heat, mass and momentum transfer in three-dimensional parabolic flows, *Int. J. Heat Mass Transfer* **15**, 1787 (1972).
52. J. P. Van Doormaal and G. D. Raithby, Enhancement of the SIMPLE method for predicting incompressible fluid flows *Numer. Heat Transfer* **7**, 147 (1984).
53. C. R. Maliska and G. D. Raithby, Calculating 3-D fluid flows using non-orthogonal grid, *Proceedings Third International Conference on Numerical Methods in Laminar and Turbulent Flows, Seattle, 1983*, pp. 656–666.
54. R. I. Issa, *Solution of the Implicit Discretized Fluid Flow Equations by Operator Splitting*, Mechanical Engineering Report, FS/82/15 (Imperial College, London, 1982).
55. J. P. Van Doormaal and G. D. Raithby, *An Evaluation of the Segregated Approach for Predicting Incompressible Fluid Flows*, ASME Paper 85-HT-9, presented at the National Heat Transfer Conference, Denver, Colorado, August 4–7, 1985.
56. S. Acharya and F. Moukalled, Improvements to incompressible flow calculation on a non-staggered curvilinear grid, *Numer. Heat Transfer. B* **15**, 131 (1989).
57. D. B. Spalding, *Mathematical Modeling of Fluid Mechanics, Heat Transfer and Mass Transfer Processes*, Mechanical Engineering Department Report, HTS/80/1 (Imperial College of Science, Technology and Medicine, London, 1980).
58. F. Moukalled and M. Darwish, A unified formulation of the segregated class of algorithms for fluid flow at all speeds, *Numer. Heat Transfer B* **37**, No. 1, 103–139, 2000.
59. C. M. Rhie, *A Numerical Study of the Flow Past an Isolated Airfoil with Separation*, Ph.D. thesis (Department of Mechanical and Industrial Engineering, University of Illinois at Urbana-Champaign, 1981).
60. S. Majumdar, Role of under-relaxation in momentum interpolation for calculation of flow with non-staggered grids, *Numer. Heat Transfer* **13**, 125 (1988).
61. R. H. Ni, A multiple grid scheme for solving the Euler equation, *AIAA J*. **20**, 1565 (1982).
62. K. P. Dimitriadis and M. A. Leschziner, A cell-Vertex TVD Scheme for transonic viscous flow, in *Numerical Methods in Laminar and Turbulent Flow*, edited by C. Taylor, J. H. Chin, and G. M. Homsy, (—, —, 1991), Vol. 7, pp. 874–885.
63. L. Stolcis and L. J. Johnston, Solution of the Euler equation on unstructured grid for two-dimensional compressible flow, *Aeronaut. J*. **94**, 181 (1990).
64. A. Brandt, Multi-level adaptive solutions to boundary-value problems, *Math. Comput*. **31**, 333 (1977).
65. H. L. Stone, Iterative solution of implicit approximations of multidimensional partial differential equations, *SIAM J. Numer. Anal*. **5**(3), 530 (1968).
66. D. Kershaw, The incomplete Cholesky-conjugate gradient method for the iterative solution of systems of linear equations, *J. Comput. Phys.* **26**, 43 (1978).
67. S. M. H. Karimian and G. E. Schneider, Application of a control-volume-based finite-element formulation to the shock tube problem, *AIAA J*. **33**(1), 165 (1994).
68. M. Darbandi and G. E. Schneider, Comparison of pressure-based velocity and momentum procedures for shock tube problem, *Numer. Heat Trans. B* **33**, 287 (1998).
69. P. H. Azoury, Engineering Applications of Unsteady Fluid Flow (Wiley, New York, 1992).